# Highly Sensitive Room-temperature $NO_2$ Sensing based on $SnO_2/WS_2$ Heterojunctions

Junyi Lin [1, 2, *], Bofeng Luo [2], Liang Zhao [2], Jiguang Zhao [2],

Qiancheng Lv [2], Zhengkai Li [2], Zhenliang Ye [2], He Wang [1, 2]

[1] CSG Digital Power Grid Research Institute Co., Ltd., Guangzhou Guangdong, 510700, China

[2] CSG Sensing Technology (Guangdong) Co., Ltd., Shenzhen Guangdong, 518102, China

* Corresponding Author: Junyi Lin

**Abstract.** Two-dimensional (2D) transition metal dichalcogenides (TMDs) have garnered attention due to their rich active sites, layered structures, and suitable electronic structures for gas sensing at room temperature. However, the sensitivity, response, recovery, stability, and selectivity of TMDs-based gas sensors remain significant challenges. Therefore, it is necessary to functionalize them to improve their gas-sensing performance at room temperature. In this work, a novel gas sensor based on 0D/2D tin oxide ($SnO_2$)/tungsten disulfide ($WS_2$) heterojunctions was rationally designed via a sol-gel process, enabling high-performance detection of nitrogen dioxide ($NO_2$) at room temperature. The ratio of $SnO_2$ in the hybrid was optimized by modulating the amount of $SnO_2$ nanoparticles. Specifically, compared with other composites with $SnO_2$ nanoparticles, the $SnO_2/WS_2$ hybrid shows the best gas-sensitive performance when the $SnO_2$ content is 30 mol%, with a response of 17.4 to 10 ppm $NO_2$, which is 4.12 times higher than that of the bare $WS_2$ gas sensor, and full recovery can be achieved. The gas sensor displays good response performance, ultra-high repeatability, and long-term stability, with excellent selectivity to $NO_2$ against other interfering gases, including $CO_2$, $NH_3$, $H_2S$, and $H_2$. Furthermore, it is demonstrated that the greatly enhanced gas sensing performance of 0D/2D $SnO_2/WS_2$ heterojunctions can be ascribed to the unique structure and the synergistic effects between $WS_2$ nanosheets and $SnO_2$ nanoparticles in terms of geometry, charge transfer, and chemical aspects. This work presents a promising methodology for the rational design of high-performance gas sensing materials for room-temperature environmental monitoring.

**Keywords:** Gas Sensor; Transition Metal Dichalcogenides; p-n Heterojunction; $NO_2$ Sensing.

## 1. Introduction

Nitrogen dioxide ($NO_2$) is a major air pollutant posing significant risks to both the environment and human health. As an acidic gas, $NO_2$ contributes to the formation of acid rain, which in turn results in the deterioration of soil and water quality[1]-[2]. Moreover, $NO_2$ contributes to the formation of tropospheric ozone, thereby exacerbating ozone pollution, which in turn affects air quality and plant growth[3]. Regarding human health, $NO_2$ is a toxic gas associated with a range of diseases, including respiratory illnesses like asthma and chronic obstructive pulmonary disease (COPD), as well as cardiovascular diseases such as heart disease, stroke, and atherosclerosis[4]-[5]. Prolonged exposure to 50 ppm $NO_2$ can irreversibly damage vital organs like heart and lungs[6]. Therefore, it is important to achieve fast and accurate detection of $NO_2$ gas. Conventional metal oxides are typically operated at high temperatures (> 240°C), which results in high energy consumption and also affects their long-term stability[7]-[10]. Therefore, there is an urgent need to develop room-temperature $NO_2$ gas sensors based on innovative nanomaterials and mechanisms.

p-Type tungsten disulfide ($WS_2$), a typical two-dimensional (2D) transition metal dichalcogenides (TMDs), has emerged as a promising candidate for room-temperature gas sensors due to its tunable electrical properties and large specific surface area[11]-[15]. Nevertheless, the lack of sufficient sensitivity and poor recovery performance represent great challenges for further applications of $WS_2$-based gas sensors. Previous research has sought to address these limitations through annealing treatments, chemical doping, exposure of edge positions, and noble metal modification. However, the

complexity of these treatments and the high material cost have hindered the development of these methods. Heterojunction design between different semiconductors is an effective method for controlling carrier concentration and improving gas sensing performance. The construction of TMDs/metal oxide semiconductor heterojunctions can effectively modulate the material resistance while promoting the adsorption of the target gas in the heterojunction, which can enhance the sensing performance. For example, Ko et al. reported that $WS_2$ nanosheets obtained through the sulfurization of the $WO_3$ atomic layer showed a response of 16% to 500 ppm $NO_2$ but with incomplete recovery[16]. Xu et al. reported the hydrothermal synthesis of $WS_2$ nanosheets for detecting $NO_2$ gas at room temperature[17]. Chen's group used a hydrothermal method to prepare $WS_2$-modified $SnO_2$ mixtures for humidity sensing [18]. However, their poor response at low concentrations renders them unsuitable for practical applications. Furthermore, the gas-sensing mechanism of the heterojunction strategy needs to be further elucidated.

The construction of 0D/2D heterojunctions allows for an increase in specific surface area, which provides a greater number of active sites for the adsorption of gas molecules and improves the efficiency of gas molecule trapping. Furthermore, the disparate energy band structures of the two materials in the 0D/2D heterojunction result in the formation of a potential barrier at the interface. This potential barrier facilitates the adsorption and desorption of gas molecules at the interface, thereby enhancing the response speed and sensitivity of the sensor[19]-[20].$SnO_2$, an n-type metal oxide with a band gap of about 3.6 eV, has been used as a sensing material for a long time[21]. In this study, unique p-n $SnO_2$/$WS_2$ heterojunctions were constructed for high-performance $NO_2$ detection. The gas sensing tests show that the gas sensor based on the $SnO_2$/$WS_2$ heterostructure exhibits excellent sensing performance for $NO_2$ detection, including high sensitivity, selectivity, full recoverability, and reliable long-term stability. It has been demonstrated that optimized p-n heterojunctions facilitate electron transport from $WS_2$ to $SnO_2$ and accelerate surface oxygen adsorption, thereby enhancing the surface catalysis of $NO_2$. The findings of this study may prove valuable in guiding the future construction of various heterojunctions for $NO_2$ detection at room temperature.

## 2. Experimental Section

### 2.1 Preparation of $WS_2$ Nanosheets

$WS_2$ nanosheets were synthesized using the liquid phase stripping method. Initially, 500 mg of bulk $WS_2$ powder was ground in a mortar with acetonitrile for 2 h. The ground powder was then dried in a vacuum oven at 60°C for 12 h to remove the excess acetonitrile. The resulting $WS_2$ powder was dispersed in 300 mL of an ethanol/water solvent mixture (35 vol%) and treated with an ultrasonic processor at 400 W for a specified time. The dispersion was centrifuged, and the supernatant was collected and further centrifuged at 8000 rpm for 30 min to obtain the $WS_2$ nanosheet precipitate. Finally, $WS_2$ nanosheets were dried under a vacuum at 60°C for 12 h to obtain $WS_2$ nanosheets.

### 2.2 Preparation of $SnO_2$ nanoparticles

$SnO_2$ nanoparticles were synthesized using the sol-gel method. Initially, 3.5 g of $SnCl_4$•$5H_2O$ was dissolved in 8 mL of deionized water. Under constant stirring, concentrated ammonia and dilute ammonia were successively added to the solution until the pH of the mixed solution reached 3. The resulting gel was then subjected to aging in a water bath at 60°C. Subsequently, the gel was alternately washed with ethanol and deionized water to remove impurities. After washing, the white gel was placed in an infrared rapid dryer for rapid drying. Finally, the dried product was placed in a muffle furnace and sintered at 550°C for 30 min to obtain $SnO_2$ nanoparticles.

### 2.3 Preparation of $SnO_2$/$WS_2$ hybrids

20 mg of the prepared $WS_2$ nanosheets were evenly dispersed in 10 mL of ethanol/water solvent mixture (35 vol%). A specific mass of $SnO_2$ nanoparticles was simultaneously dispersed in anhydrous

ethanol and ultrasonically dispersed for 30 min. Subsequently, the $SnO_2$ dispersion was slowly added dropwise into the $WS_2$ dispersion under continuous stirring. The mixed solution was ultrasonically treated for 4 h. Based on the molar fraction of $SnO_2$ to $WS_2$, the final products were named as SW-1, SW-3, SW-5, and SW-10, corresponding to 10 mol%, 30 mol%, 50 mol%, and 100 mol% of $SnO_2$, respectively. The final products were obtained by centrifugal washing with water and ethanol several times followed by vacuum drying at 60°C for 12 h.

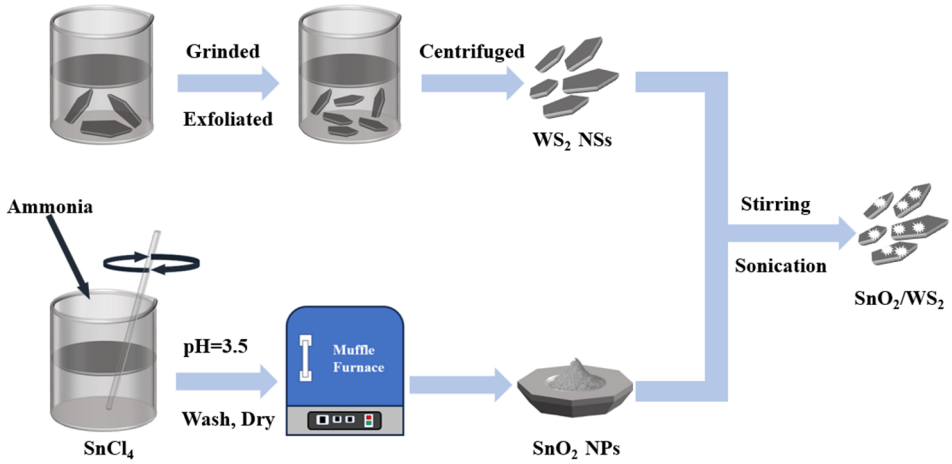


**Fig 1.** Schematic diagram of the preparation of $SnO_2/WS_2$ hybrid material.

### 2.4 Characterization

Characterization was carried out by field emission scanning electron microscopy (SEM, Ultra Plus, Carl Zeiss, Germany) and transmission electron microscopy (TEM, JEM-2010HT, JEOL, Japan). X-ray diffraction (XRD, D8 Advance, Bruker, Germany) was carried out over a wide angular range ($2\theta$ =10°–90°) by Cu-Kα radiation ($\lambda$ = 0.15418 nm). A scanning rate of 10°/min was used to investigate the crystal structure of the sensitive material. The polymorphism of the sensitive materials was investigated using a confocal Raman microscope (inVia Reflex, RENISHAW, UK) equipped with a 532 nm laser. The valence states were investigated by X-ray photoelectron spectroscopy (XPS, Kratos). The specific surface area was studied using a Bruner-Emmett-Teller instrument (BET, Micro-Teller, Meristics ASAP 2020M, USA). The band gap was measured by ultraviolet-visible spectroscopy (UV-vis, Lamda 950, PerkinElmer, USA) using diffuse reflector optics. The positions of the Fermi level and the valence band were probed by UV photoelectron spectroscopy (UPS, Kratos AXIS UltraDLD, Japan).

### 2.5 Preparation and Testing of Gas Sensors

The fabrication process of the gas sensor device is shown in Figure 2, and the interdigitated electrodes are mainly prepared by photolithography and lift-off micromachining process[22]. The size of the electrodes is 690 μm×730 μm with a finger spacing of 20 μm. To fabricate the electrodes, a 20 nm layer of titanium (Ti) and a 180 nm layer of gold (Au) were sequentially deposited onto a patterned $Si/SiO_2$ substrate via sputtering. After that, 4 μL of the prepared $SnO_2/WS_2$ hybrid dispersion was taken onto the electrodes using a pipette and dried in a vacuum oven at 60°C for 2 h. The above process was repeated multiple times to ensure the formation of a uniform layer of sensing material on the electrode surface.

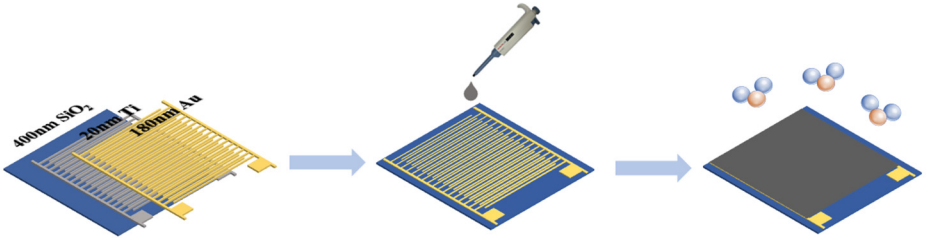


**Fig 2.** Schematic diagram of the fabrication process of interdigital electrodes and gas sensors.

### 2.6 Gas Sensing Test Systems

The schematic diagram of the gas sensor performance testing system in this work is shown in Figure 3, which mainly consists of a gas distribution system and a data acquisition system[23]. The gas distribution system regulates the ratio of target gas and compressed air in the test chamber through a mass flow controller (MFC) to dilute a fixed concentration of target gas to the required concentration for the test. The basic test procedure is as follows. Firstly, the sensor is placed in the test chamber and a background gas (air) is continuously fed into the chamber until the sensor's current stabilizes. The background gas valve is closed, and the target gas and dilution gas (air) valves are opened. The MFC is used to adjust the ratio of the two gases, achieving the required concentration of the gas mixture in the test chamber. This mixture is flowed for 100 s. Afterward, the target gas valve is closed, and the background gas valve is reopened to purge the test chamber until the sensor returns to its baseline state. When the target gas comes into contact with the sensitive material on the gas sensor, the conductivity of the sensitive material changes, which is in turn recorded in real-time by the semiconductor tester (Agilent 4156C) and displayed on the computer[24]-[27]. In this work, the response is calculated from Response = $(I_g-I_a)/I_g$, where $I_g$ and $I_a$ denote the current of the sensor in the target gas and air, respectively. Response time and recovery time are defined as the time required for the current change of the sensor to reach 90% of the total change, respectively[28].

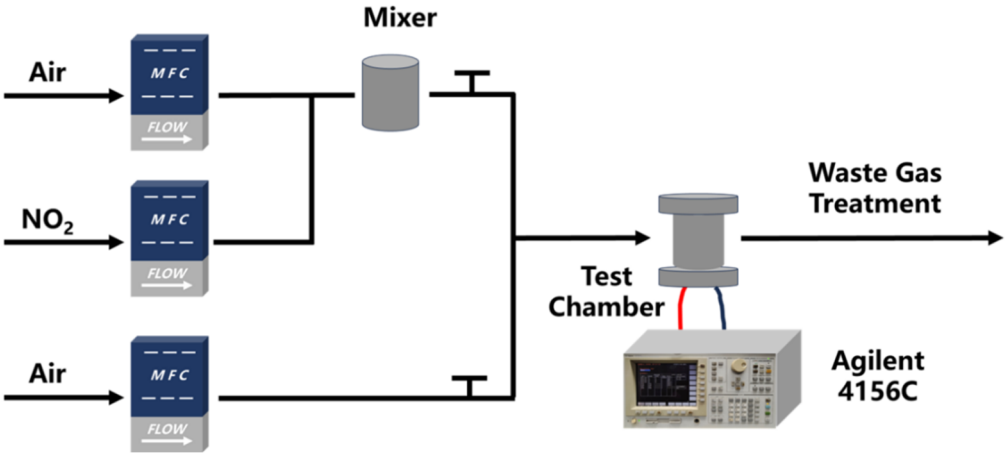


**Fig 3.** Schematic illustration of the gas sensing test system.

## 3. Results and Discussion

### 3.1 Microscopic Characterization of $SnO_2$ /$WS_2$ Hybrids.

The SEM images of the hybrid material are shown in Figure 4. The sample exhibits a 0D/2D heterogeneous structure. In Figure 4(a), no obvious loaded particles could be observed on the surface of $WS_2$ nanosheets when the content of $SnO_2$ is 10 mol%; With the increase of $SnO_2$ content, more clusters consisting of $SnO_2$ nanoparticles could be observed on the surface of $WS_2$ nanosheets. In Figure 4(b)(c), when the $SnO_2$ content reaches 30 mol% and 50 mol%, the size of $SnO_2$ nanoparticle clusters is smaller and more uniformly distributed. However, In Figure 4(d), at a $SnO_2$ content of 100 mol%, the nanoparticles tend to aggregate, resulting in larger cluster sizes.

The hybrid material exhibits a complex microstructure, as shown in the TEM images in Figure 5. Figure 5(a) reveals that the hybrid primarily consists of stacked $WS_2$ nanosheets and agglomerated $SnO_2$ nanoparticle clusters. Some $SnO_2$ nanoparticles are in contact with the $WS_2$ nanosheets, forming a heterostructure. This observation is further confirmed by the HRTEM image in Figure 5(b), where a lattice fringe spacing of 0.27 nm is identified, corresponding to the (100) crystallographic plane of 2H-$WS_2$. A lattice stripe spacing of 0.34 nm can also be observed on $SnO_2$ nanoparticles, which corresponds to the (110) crystallographic surface of $SnO_2$. In addition, a certain degree of lattice distortion can be observed at the junction, which further confirms the creation of heterogeneous structures. The SAED image in Figure 5(c) also displays hexagonal diffraction spots for $WS_2$ and

additional spots with a lattice spacing of 0.34 nm, further confirming the successful integration of $SnO_2$ nanoparticles onto $WS_2$ nanosheets.

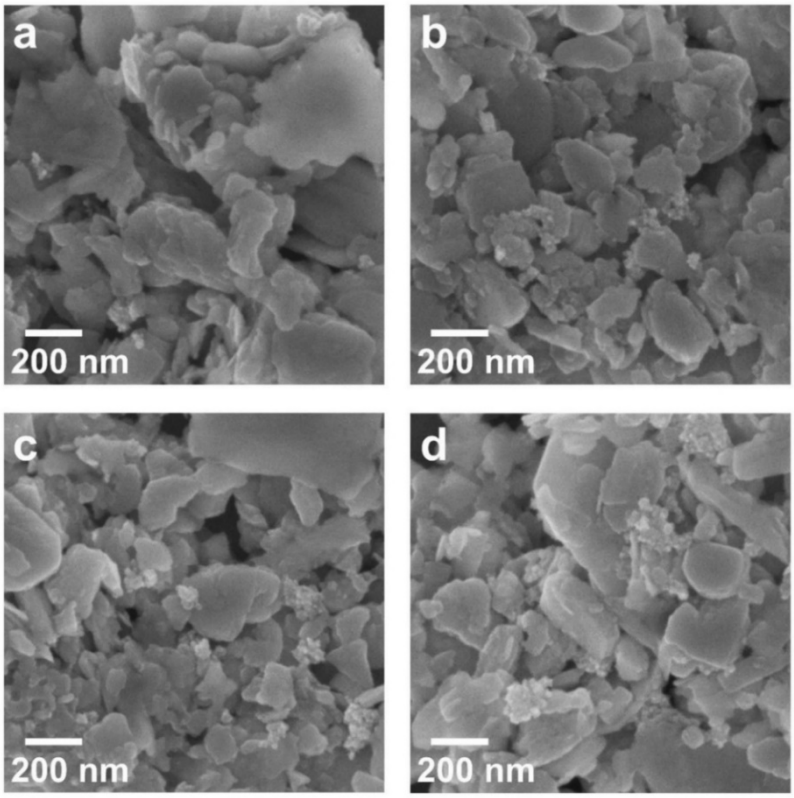


**Fig 4.** SEM images of $SnO_2/WS_2$ hybrid material with different $SnO_2$ contents. (a) SW-1; (b) SW-3; (c) SW-5; (d) SW-10

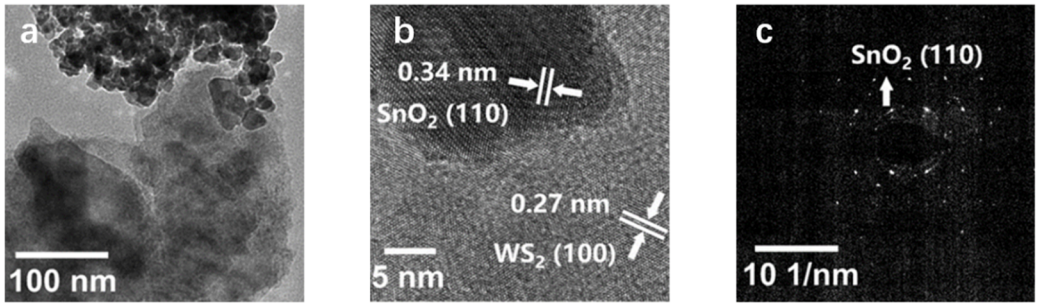


**Fig 5.** Morphologies of SW-3. (a) TEM image of SW-3; (b) HRTEM image of SW-3; (c) SAED image of SW-3.

The crystallographic information of $SnO_2/WS_2$ hybrids can be observed from the XRD pattern in Fig.6(a). The diffraction peaks of $WS_2$ nanosheets perfectly align with those of 2H-$WS_2$ (JCPDS No. 84-1398), with no additional peaks observed, indicating the high crystallinity and purity of the exfoliated $WS_2$ nanosheets. In the XRD pattern of SW-3, in addition to the diffraction peaks corresponding to $WS_2$, the diffraction peaks are mainly matched with the diffraction peaks of $SnO_2$ (JCPDS No. 41-1445) with crystal planes corresponding to (110), (101), and (211), which indicates the successful formation of $SnO_2$ /$WS_2$ heterostructure.

XPS further characterized the elemental composition and chemical states of $SnO_2/WS_2$ hybrids. The XPS full spectra of $WS_2$ nanosheets and SW-3 are demonstrated in Figure 6(b). The spectrum of $WS_2$ primarily exhibits peaks corresponding to W and S elements. In contrast, the XPS spectrum of

SW-3, in addition to the W and S peaks from $WS_2$, also displays Sn 3d peaks, thereby confirming the presence of Sn in the composite material.

The XPS fine spectra corresponding to the elements W, S, Sn, and O in the hybrids are further demonstrated in Figs.6(c–f). Figure 6(c) shows the fine spectra of $WS_2$ and W 4f of SW-3, which shows that the three characteristic peaks of SW-3 at 32.55, 34.73, and 37.96 eV correspond to W $4f_{7/2}$, W $4f_{5/2}$, and W $5p_{3/2}$, respectively. The peak at 35.78 eV corresponds to the W-O peak, suggesting oxidation due to oxygen adsorption from air. However, no significant oxidation peaks are observed in the XRD patterns, indicating that only a minor amount of $WS_2$ is oxidized, which is negligible [29]. Figure 6(d) shows two main peaks in SW-3, corresponding to S $2p_{3/2}$ and S $2p_{1/2}$ at 162.22 and 163.32 eV, respectively. In $WS_2$, the W 4f peaks are located at 32.70, 34.86, and 38.06 eV, and the S 2p peaks are at 162.30 and 163.35 eV. The shift of W 4f and S 2p peaks in SW-3 to lower binding energies compared to $WS_2$ suggests an increase in the electron cloud density around $WS_2$, indicating electron transfer from $SnO_2$ to $WS_2$ and confirming the formation of the $SnO_2/WS_2$ heterostructure. The Sn 3d spectra in Figure 6(e) shows a peak separation of 8.4 eV, indicating that Sn exists in the form of $Sn^{4+}$ ions[29]. Finally, the O 1s spectra in Figure 6(f) show a peak at 531.02 eV, corresponding to the Sn-O bond, while the higher binding energy peak represents oxygen in surface hydroxyl groups [31].

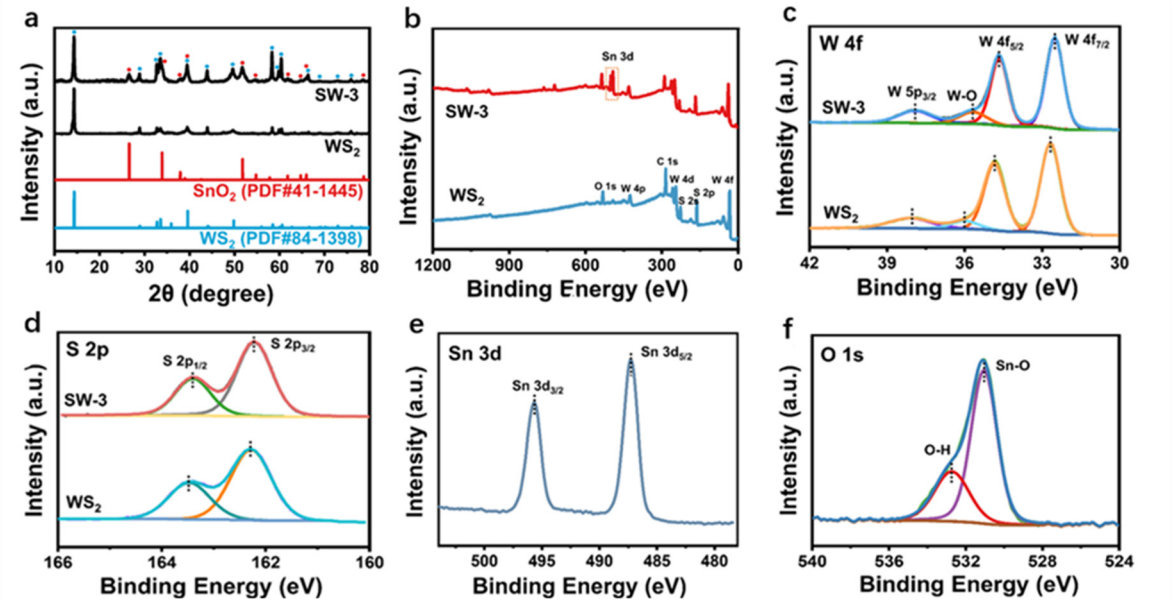


**Fig 6.** The fine spectra of $WS_2$ nanosheets and SW-3 elements.(a) XRD patterns of $WS_2$ nanosheets and SW-3; (b) Full XPS spectra of $WS_2$ nanosheets and SW-3; High-resolution XPS spectra of (c) W 4f, (d) S 2p, (e) Sn 3d and (f) O 1s of $WS_2$ nanosheets and SW-3, respectively.

### 3.2 Sensing Performance Analysis

The prepared $SnO_2/WS_2$ hybrids were fabricated for gas sensor devices and tested for gas sensing of $NO_2$ using a gas sensing test system at room temperature. The temperature was maintained at 25 °C, the concentration of $NO_2$ was 10 ppm, and the ventilation time was uniformly controlled at 100 s. The obtained gas sensing response results are shown in Figure 7. Firstly, it can be seen that the response of the compliant material to 10 ppm of $NO_2$ gas is increased from 3.40 to over 10 compared with the gas sensor made of pure $WS_2$ nanosheets. Moreover, the modification of $SnO_2$ nanoparticles also effectively enhances the recovery performance of $WS_2$ nanosheets at room temperature, and it can be seen from the figure that the hybrids with different $SnO_2$ ratios can recover to the baseline. Finally, the hybrid SW-3 obtained with a 30 mol% $SnO_2$ ratio has a relatively better response and recovery performance, achieving a maximum response of 17.4 while maintaining excellent recovery behavior.

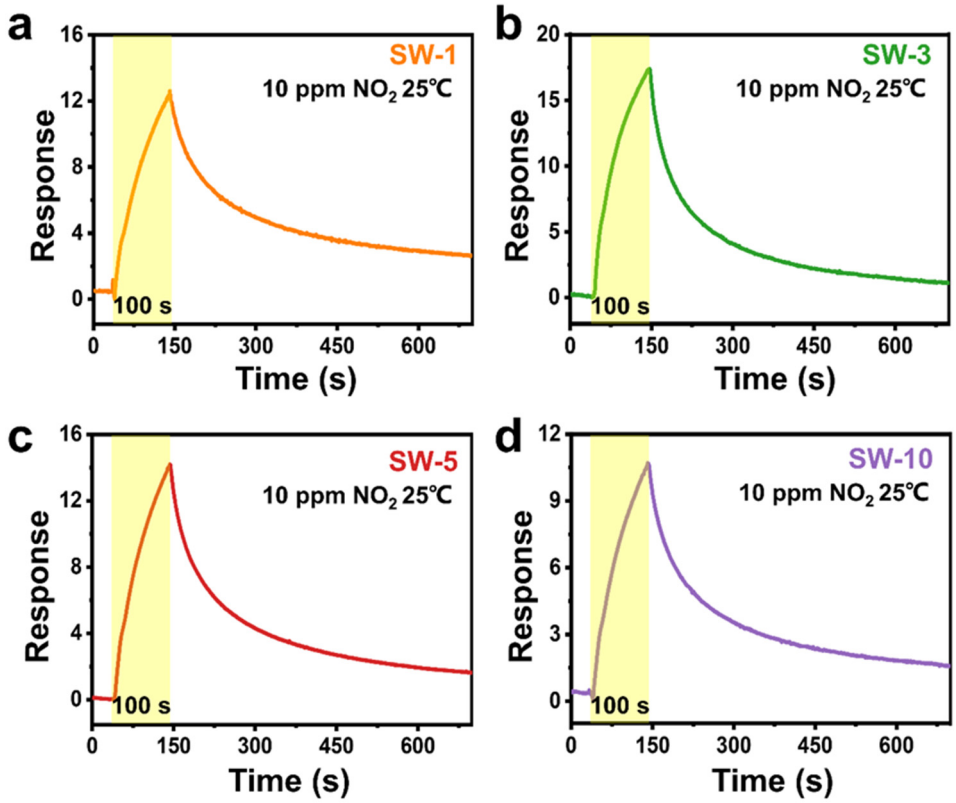


**Fig 7.** Response of (a) SW-1, (b) SW-3, (c) SW-5, and (d) SW-10 to $NO_2$ at room temperature.

Figure 8(a) compares the response of $WS_2$ nanosheets and $SnO_2/WS_2$ hybrids with different $SnO_2$ contents to 10 ppm $NO_2$. The effect of the modification of $SnO_2$ nanoparticles on the $WS_2$ nanosheet gas sensor is illustrated more clearly in Figure 8(b).

The response of the SW-3 gas sensor reaches 17.4 for 10 ppm $NO_2$, representing an improvement by a factor of 4.12 over that of pure $WS_2$ nanosheets. This enhancement is attributed to the optimal $SnO_2$ content. Excessive $SnO_2$ can lead to nanoparticle agglomeration, which in turn reduces the number of available adsorption sites and consequently the response. The figure also shows that after 500 s of recovery, the SW-3 gas sensor recovers more than 90%, while the $WS_2$ nanosheet sensor recovers less than 50%. Therefore, SW-3 was selected as the primary focus for subsequent tests. Figure 8(c) depicts the dynamic response of SW-3 to different concentrations of $NO_2$ gas, with a controlled venting time of 20 s to enhance the testing efficiency. It is evident that as the gas concentration increases, the response of the SW-3 sensor also rises. A linear fitting of the relationship between $NO_2$ concentration and the change in response was performed, and the results obtained are shown in Figure 8(d). The fitting results show that the SW-3 gas sensor has a good linear relationship between concentration and response. In addition, according to $LOD = 3 \times S_{\text{Standard Error}}/K_{\text{Slope}}$, it can be deduced that the theoretical detection limit of the SW-3 gas sensor for $NO_2$ is 522 ppb[32].

In addition to the response, the parameters of the gas sensor such as repeatability, long-term stability, humidity effect, and selectivity are important for practical use. As shown in Figure 9(a), after five cycle tests, the response of the SW-3 gas sensor to 10 ppm $NO_2$ was the same, with slight fluctuations, proving good repeatability and cycle stability. The long-term stability of the SW-3 gas sensor was then tested for 18 days, with the response to 10 ppm $NO_2$ tested every 3 days. The plotted long-term stability image in Figure 9(b) shows the response to 10 ppm $NO_2$ is maintained at around 17.4 over time, indicating relatively reliable long-term stability. For room temperature gas sensors, humidity also significantly affects sensor performance. Therefore, the response performance of the SW-3 gas sensor to 10 ppm $NO_2$ gas was tested under different relative humidity (RH) controlled at 10%RH, 30%RH, 50%RH, 70%RH, and 90%RH. The measured response in Figure 9(c) show the response decreases with the increasing RH. This is due to more water molecules occupying the active

sites of gas molecule adsorption, reducing the number of adsorbed gas molecules and consequently decreasing the response [33]. However, even with 70%RH, the SW-3 gas sensor has a response of 6.86, higher than that of the pure $WS_2$ gas sensor, showing good response performance at high humidity. Finally, to test the selectivity of the SW-3 gas sensor, it was exposed to 10 ppm of $NO_2$, $CO_2$, $NH_3$, $H_2S$, and $H_2$, respectively, and the response was recorded and plotted in a bar graph as shown in Figure 9(d). The response for 10 ppm $NO_2$ is much higher than for other gases of the same concentration, showing excellent selectivity toward $NO_2$.

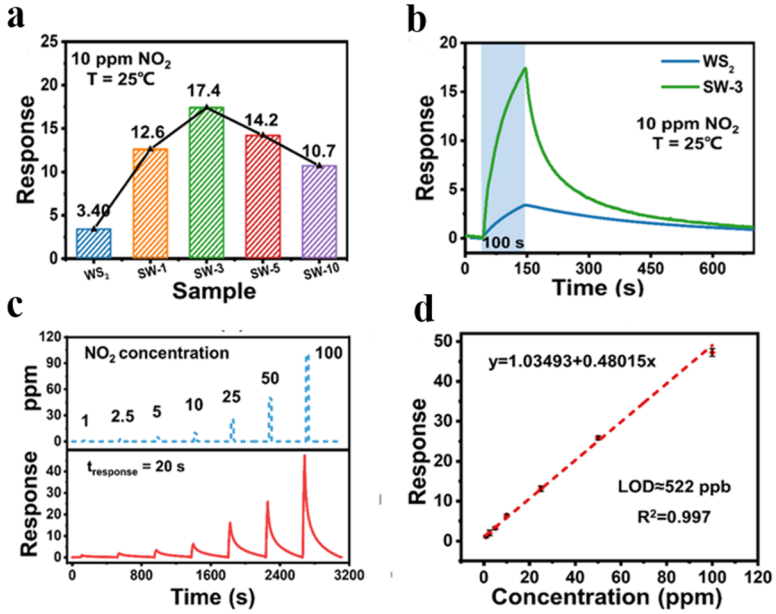


**Fig 8.** Sensing performance of the gas sensors to $NO_2$. (a) Response of $WS_2$, SW-1, SW-3, SW-5, and SW-10 to 10 ppm $NO_2$; (b) Response of $WS_2$ nanosheets and SW-3 to $NO_2$; (c) Response/recovery transients of SW-3 to 1-100 ppm $NO_2$; (d) The relationships between the response and the concentration of $NO_2$ based on SW-3.

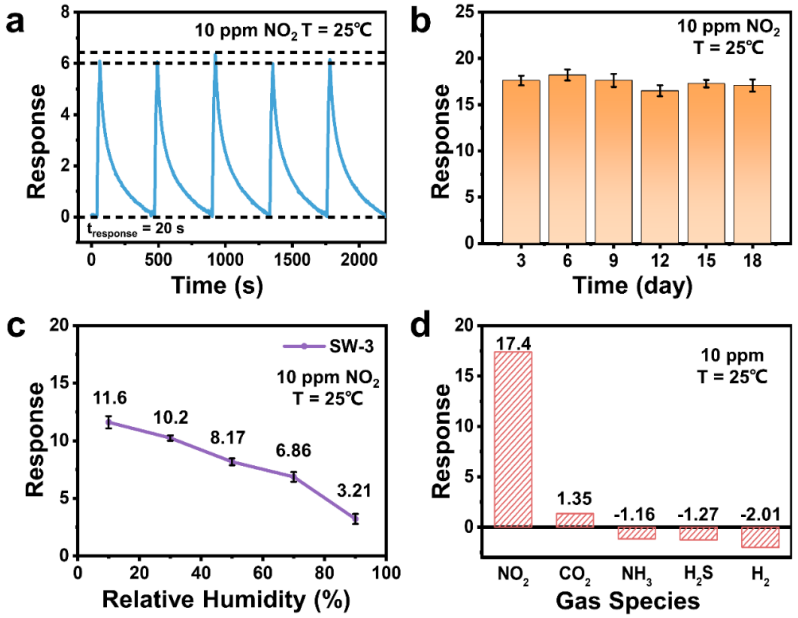


**Fig 9.** Stability and selectivity performance of SW-3 gas sensor. (a) Five successive cycles of SW-3 gas sensor to 10 ppm $NO_2$; (b) Long-term stability of SW-3 gas sensor to 10 ppm $NO_2$; (c) Response of SW-3 gas sensor to 10 ppm $NO_2$ under different relative humidity conditions; (d) The selectivity of SW-3 gas sensor to 10 ppm $NO_2$ gas sensor to 10 ppm $NO_2$, $CO_2$, $NH_3$, $H_2S$, and $H_2$.

### 3.3 Sensing Mechanism Analysis

The improvement in the $NO_2$ sensing performance of the above $SnO_2/WS_2$ hybrids at room temperature is mainly attributed to the formation of a p-n heterojunction between $SnO_2$ and $WS_2$. The main gas sensing mechanism is described as follows, and the sensing mechanism of the $SnO_2/WS_2$ hybrids for $NO_2$ gas sensing is also plotted in Fig. 10(a). $WS_2$ nanosheets are p-type semiconductors with holes as the main carriers, while the $SnO_2$ nanoparticles are n-type semiconductors with electrons as the main carriers. When $SnO_2$ is in contact with $WS_2$, the main carriers will migrate to each other to balance the Fermi energy levels due to the thermal difference in Fermi energy levels. This means that holes of the p-type semiconductor $WS_2$ will be transferred to the n-type semiconductor $SnO_2$, while electrons of the n-type semiconductor $SnO_2$ will be transferred to the surface of the p-type semiconductor $WS_2$. This process results in a built-in electric field at the interface between $SnO_2$ and $WS_2$, which bends the energy bands and prevents further diffusion of carriers, as shown in Fig. 10(b).

When the $SnO_2/WS_2$ hybrids are exposed to the $NO_2$ gas environment, the $NO_2$ gas molecules capture electrons from the $SnO_2$ nanoparticles, forming $NO_2^-$. This disrupts the equilibrium of the built-in electric field at the p-n junction, and the excess holes go back to the $WS_2$ nanosheets, resulting in a new equilibrium state. This reduces the width of the potential barriers at the interface and increases the electrical conductivity of the $SnO_2/WS_2$ hybrids. Moreover, since $WS_2$ is a p-type semiconductor, more holes can also enhance the conductivity of $WS_2$, increasing the response to $NO_2$. Furthermore, the 0D/2D structure formed by the $SnO_2/WS_2$ heterojunctions avoids large-scale agglomerate stacking of $SnO_2$ nanoparticles and $WS_2$ nanosheets, increasing the specific surface area and number of active sites and thus enhancing the gas sensing performance[34].

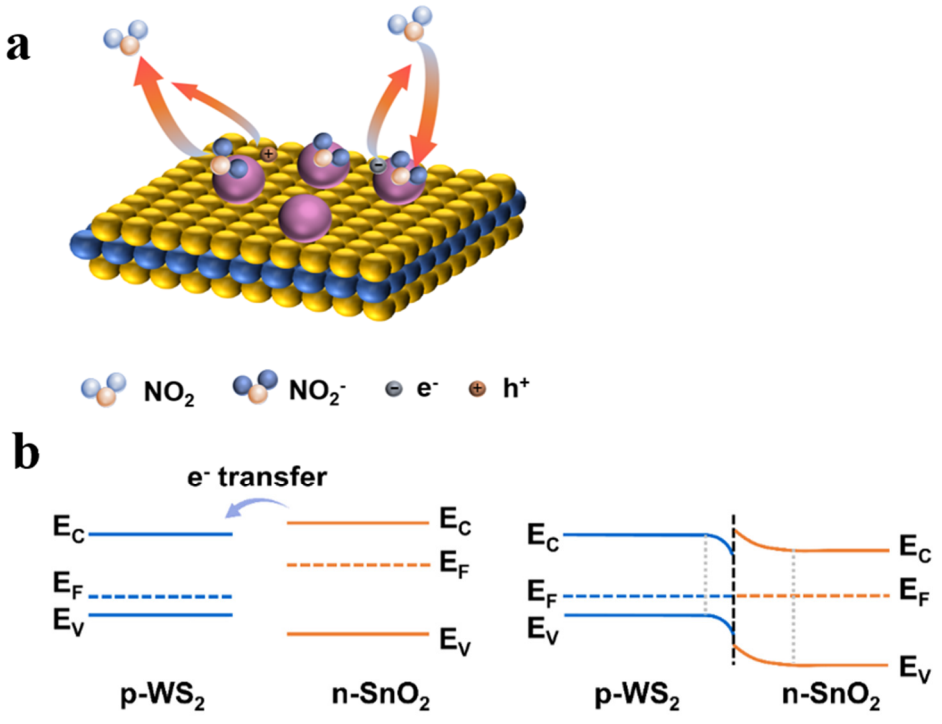


**Fig 10.** The enhancement mechanism of $SnO_2/WS_2$ hybrid material. (a) Schematic illustration of the charge transfer process and gas sensing mechanisms. (b) Energy band structures of $SnO_2/WS_2$ heterojunctions before and after contact with the hybrid material.

## 4. Conclusion

In this study, we have designed a novel 0D/2D $SnO_2/WS_2$ heterojunction-based gas sensor, which exhibits excellent sensitivity and recoverability for $NO_2$ detection at room temperature. The optimized

$SnO_2/WS_2$ sensor performs a sensitivity of 17.4 to 10 ppm $NO_2$. More importantly, 0D/2D $SnO_2/WS_2$ heterostructures-based gas sensors can be completely recovered without using any external auxiliary treatments. Besides, the 0D/2D $SnO_2/WS_2$-based gas sensor also performs high selectivity and outstanding stability. The enhanced sensing performance of 0D/2D $SnO_2/WS_2$ heterostructures can be attributed to the formed p-n heterojunctions, enriched active sites, improved charge transfer, and the synergistic effects between $WS_2$ nanosheets and $SnO_2$ nanoparticles. This work can shed light on the rational design of high-performance room-temperature gas sensing systems by delicately constructing p-n heterojunctions.

## Acknowledgments

This work was supported by the National Key Research and Development Program of China (2022YFB3205500), the National Natural Science Foundation of China (62371299 and 62101329), and the Natural Science Foundation of Shanghai (23ZR1430100). We also acknowledge analysis support from the Instrumental Analysis Center of Shanghai Jiao Tong University and the Center for Advanced Electronic Materials and Devices of Shanghai Jiao Tong University. The computations in this paper were run on the π 2.0 cluster supported by the Center for High-Performance Computing at Shanghai Jiao Tong University.

## References

[1] P. Grennfelt, A. Engleryd, M. Forsius, et al. Acid rain and air pollution: 50 years of progress in environmental science and policy[J]. Ambio, 2020, 49(4): 849–864.

[2] D. Fowler, J. N. Cape, I. D. Leith, et al. Rainfall acidity in northern Britain[J]. Nature, 1982, 297(5865): 383–385.

[3] T. Wang, L. Xue, P. Brimblecombe, et al. Ozone pollution in China: A review of concentrations, meteorological influences, chemical precursors, and effects[J]. Science of The Total Environment, 2017, 575: 1582–1596.

[4] F. Hu, Y. Guo. Health impacts of air pollution in China[J]. Frontiers of Environmental Science & Engineering, 2020, 15(4): 74.

[5] H. Salonen, T. Salthammer, L. Morawska. Human exposure to $NO_2$ in school and office indoor environments[J]. Environment International, 2019, 130: 104887.

[6] Y. Guan, Y. Xiao, C. Chu, et al. Trends and characteristics of ozone and nitrogen dioxide-related health impacts in Chinese cities[J]. Ecotoxicology and Environmental Safety, 2022, 241: 113808.

[7] V. Schroeder, S. Savagatrup, M. He, et al. Carbon nanotube chemical sensors[J]. Chemical Reviews, 2019, 119(1): 599–663.

[8] D.R. Miller, S.A. Akbar, P.A. Morris. Nanoscale metal oxide-based heterojunctions for gas sensing: A review[J]. Sensors and Actuators B: Chemical, 2014, 204: 250–272.

[9] Q. Li, J. Meng, Z. Li. Recent progress on Schottky sensors based on two-dimensional transition metal dichalcogenides[J]. Journal of Materials Chemistry A, 2022, 10(15): 8107–8128.

[10] Q. Wang, J. Sun, D. Wei. Two-dimensional metal-organic frameworks and covalent organic frameworks[J]. Chinese Journal of Chemistry, 2022, 40(11): 1359–1385.

[11] Lee E., Yoon Y. S., Kim D. J. Two-dimensional transition metal dichalcogenides and metal oxide hybrids for gas sensing[J]. ACS Sensors, 2018, 3(10): 2045-2060.

[12] Han Y, Liu Y, Su C, et al. Interface-engineered $WS_2$/ZnS heterostructures for sensitive and reversible $NO_2$ room temperature sensing[J]. Sensors and Actuators B: Chemical, 2019, 296: 126666.

[13] Liu X, Hu J, Yue C, et al. High-performance field-effect transistor based on multilayer tungsten disulfide[J]. ACS Nano, 2014, 8(10): 10396-10402.

[14] Zhang D, Liu T, Cheng J, et al. Lightweight and high-performance microwave absorber based on 2D $WS_2$–RGO heterostructures[J]. Nano-Micro Letters, 2019, 11: 1-15.

[15] Alagh A, Annanouch F E, Umek P, et al. CVD growth of self-assembled 2D and 1D $WS_2$ nanomaterials for the ultrasensitive detection of $NO_2$[J]. Sensors and Actuators B: Chemical, 2021, 326: 128813.

[16] Ko K Y, Song J G, Kim Y, et al. Improvement of gas-sensing performance of large-area tungsten disulfide nanosheets by surface functionalization[J]. ACS nano, 2016, 10(10): 9287-9296.

[17] Xu T, Liu Y, Pei Y, et al. The ultra-high $NO_2$ response of ultra-thin $WS_2$ nanosheets synthesized by hydrothermal and calcination processes[J]. Sensors and Actuators B: Chemical, 2018, 259: 789-796.

[18] Chen, Yunpeng, et al. Humidity sensing properties of the hydrothermally synthesized $WS_2$-modified $SnO_2$ hybrid nanocomposite. Applied Surface Science 447 (2018): 325-330.

[19] Bag A, Lee N E. Gas sensing with heterostructures based on two-dimensional nanostructured materials: a review[J]. Journal of Materials Chemistry C, 2019, 7(43): 13367-13383.

[20] Goel N, Kushwaha A, Kwoka M, et al. Mixed-dimensional van der Waals heterostructures enabled gas sensors: Fundamental and Application[J]. Journal of Materials Chemistry A, 2024.

[21] Dieguez A, Romano-Rodrıguez A, Vila A, et al. The complete Raman spectrum of nanometric SnO 2 particles[J]. Journal of Applied Physics, 2001, 90(3): 1550-1557.

[22] Z. Sun, D. Huang, Z. Yang, et al. ZnO nanowire-reduced graphene oxide hybrid-based portable $NH_3$ gas sensing electron device[J]. IEEE Electron Device Letters, 2015, 36(12): 1376–1379.

[23] R. Guo, Y. Han, C. Su, et al. Ultrasensitive room temperature $NO_2$ sensors based on liquid-phase exfoliated $WSe_2$ nanosheets[J]. Sensors and Actuators B: Chemical, 2019, 300: 127013.

[24] Huang D, Li X, Wang S, et al. Three-dimensional chemically reduced graphene oxide templated by silica spheres for ammonia sensing[J]. Sensors and Actuators B: Chemical, 2017, 252: 956–964.

[25] Huang D, Yang Z, Li X, et al. Three-dimensional conductive networks based on stacked $SiO_2$@ graphene frameworks for enhanced gas sensing[J]. Nanoscale, 2017, 9(1): 109–118.

[26] Yang Z, Cao W, Peng C, et al. Construction, application, and verification of a novel formaldehyde gas sensor system based on Ni-doped $SnO_2$ nanoparticles[J]. IEEE Sensors Journal, 2021, 21(9): 11023–11030.

[27] Sun Z, Huang D, Yang Z, et al. ZnO nanowire-reduced graphene oxide hybrid-based portable $NH_3$ gas sensing electron device[J]. IEEE Electron Device Letters, 2015, 36(12): 1376–1379.

[28] Chen X, Wang S, Su C, et al. Two-dimensional Cd-doped porous $Co_3O_4$ nanosheets for enhanced room-temperature $NO_2$ sensing performance[J]. Sensors and Actuators B: Chemical, 2020, 305: 127393.

[29] Y. Han, D. Huang, Y. Ma, et al. Design of hetero-nanostructures on $MoS_2$ nanosheets to boost $NO_2$ room-temperature sensing[J]. ACS Applied Materials & Interfaces, 2018, 10(26): 22640–22649.

[30] M. Kwoka, L. Ottaviano, M. Passacantando, et al. XPS study of the surface chemistry of L-CVD $SnO_2$ thin films after oxidation[J]. Thin Solid Films, 2005, 490(1): 36–42.

[31] C. Tan, H. Zhang. Epitaxial growth of hetero-nanostructures based on ultrathin two-dimensional nanosheets[J]. Journal of the American Chemical Society, 2015, 137(38): 12162–12174.

[32] Y. Niu, J. Zeng, X. Liu, et al. A photovoltaic self-powered gas sensor based on all-dry transferred $MoS_2$/GaSe heterojunction for ppb-level $NO_2$ sensing at room temperature[J]. Advanced Science, 2021, 8(14): 2100472.

[33] C. Liu, X. Chen, H. Luo, et al. Highly sensitive and recoverable room-temperature $NO_2$ gas detection realized by 2D/0D $MoS_2$/ZnS heterostructures with synergistic effects[J]. Sensors and Actuators B: Chemical, 2021, 347: 130608.

[34] J. Hu, C. Zou, Y. Su, et al. An ultrasensitive $NO_2$ gas sensor based on a hierarchical $Cu_2O$/CuO mesocrystal nanoflower[J]. Journal of Materials Chemistry A, 2018, 6(35): 17120–17131.